Rakenteiden Mekaniikka (Journal of Structural Mechanics)
Vol. 48, No 2, 2015, pp. 99 – 114
rmseura.tkk.fi/rmlehti/

VERTAISARVIOITU
KOLLEGIALT GRANSKAD
PEER-REVIEWED
www.tsv.fi/tunnus

Damage-viscoplastic model based on the Hoek-Brown criterion for numerical modeling of rock fracture

Timo Saksala

Summary. This article presents a phenomenological damage-viscoplastic model based on the empirical Hoek-Brown criterion for numerical modeling of rock fracture. The viscoplastic part of the model is formulated in the spirit of the consistency model by Wang (1997). Isotropic damage model with separate damage variables in tension and compression is employed to describe the stiffness and strength degradation. The model is implemented with the FE method using the constant strain triangle elements. The equations of motion are solved with the explicit time marching scheme. In the numerical examples, after demonstrating the model response at the material point level, confined compression and uniaxial tension tests on rock are simulated as quasi-static problems. Moreover, the dynamic three-point bending of a notched semicircular disc test is simulated in order to demonstrate the model predictions under dynamic loading conditions.

Key words: Hoek-Brown criterion, viscoplastic consistency model, isotropic damage, finite element method, rock fracture

Received 17 February 2015. Accepted 23 June 2015. Published online 20 November 2015

Introduction

Numerical modeling of rock fracture is an active area of research in the field of computational mechanics due to its importance in failure analyses of underground rock structures and rock breakage industry. The major challenges therein are related to numerical modeling of crack propagation and numerical description of rock micro-structure. Many numerical models, based on the finite element method and the discrete element method, have been developed during the last decades for the simulation of rock fracture. For a review article on numerical methods in rock mechanics, see [1].

In the present paper the continuum approach based on the finite element method is chosen due to its computational efficiency and maturity as a numerical method. It will be seen that despite its underlying principle of treating materials as a continuous medium, it can be successfully, in the engineering sense, employed in modeling crack propagation under dynamic and quasi-static loading conditions even in brittle materials such as rock. For this end, a constitutive model based on a combination of the isotropic damage concept [3] and viscoplastic consistency model by Wang et al. [2] is developed.

The damage part of the model with separate damage variables in tension and compression describes the stiffness and strength degradation of the material under loading.

The viscoplastic part of the model, which governs the inelastic strain development and the strain-rate dependency, is based on the Hoek-Brown failure criterion for rocks [4]. The choice of this criteria is justified based on the test data and implementation economy and simplicity grounds. The damage and viscoplastic parts are combined with the effective stress space formulation [5]. The model is implemented in explicit dynamics FE setting.

The model predictions are demonstrated first at the material point level simulation using a single constant strain triangle element. Then the model is tested at the laboratory sample level in 2D simulations. First, the confined compression and uniaxial tension tests on rock are simulated. Second, dynamic three-point bending test of a notched semicircular rock sample is simulated as a transient problem involving contact.

Theory of the material model for rock

The theory of the model is presented here. First, the viscoplastic part of the model based on the viscoplastic consistency approach is formulated. Then, the isotropic damage model is developed for present purposes. The model components are combined with the effective stress space approach. The details of stress integration are also presented for the convenience of the reader. Third, the explicit time integration method for solving the equations of motion is presented. Finally, the statistical modeling of rock strengths based on the Weibull distribution is briefly sketched.

Viscoplasticity part of the model

Classical viscoplasticity formulations, such as the Perzyna model, do not utilize the consistency condition. Consequently, a trial stress state violating the yield criterion is not returned to the yield surface. However, Wang et al. [2] presented a so-called viscoplastic consistency model which utilizes the consisteny condition and thus recasts the viscoplasticity theory into the classical computational plasticity format. The major difference of this formulation to the classical plasticity models is the dependence of the yield function on the rate of the internal variables. The main ingredients of such a model are

$$f_{\mathrm{vp}} = f(\boldsymbol{\sigma}, \kappa, \dot{\kappa}), \tag{1}$$

$$\dot{\boldsymbol{\epsilon}}^{\mathrm{vp}} = \dot{\lambda}\frac{\partial g_{\mathrm{vp}}}{\partial \boldsymbol{\sigma}}, \quad \dot{\kappa} = \dot{\lambda}k(\boldsymbol{\sigma}, \kappa), \tag{2}$$

$$f_{\mathrm{vp}} \leq 0, \quad \dot{\lambda} \geq 0, \quad \dot{\lambda} f_{\mathrm{vp}} = 0, \tag{3}$$

where $\boldsymbol{\sigma}$ is the stress tensor, g_{vp} is the viscoplastic potential, f_{vp} is the dynamic yield function, κ, $\dot{\kappa}$ are the internal variable and its rate, respectively, $\dot{\lambda}$ is the viscoplastic increment and $k(\boldsymbol{\sigma}, \kappa)$ is a function relating the rates of κ and λ. Equation (2) expresses the non-associated flow rule (the associated case is obtained by $g_{\mathrm{vp}} = f_{\mathrm{vp}}$) while Equation (3) states the Kuhn-Tucker loading-unloading conditions. Finally, as rocks are brittle materials, the present model can be formulated under the assumption of small deformations (and rigid body rotations). Therefore, the decomposition of the total strain rate into elastic and viscoplastic parts

$$\dot{\boldsymbol{\epsilon}} = \dot{\boldsymbol{\epsilon}}^{\mathrm{e}} + \dot{\boldsymbol{\epsilon}}^{\mathrm{vp}} \tag{4}$$

is performed here as in the rate independent plasticity.

The consistency condition becomes

$$\dot{f}_{\mathrm{vp}}(\boldsymbol{\sigma}, \kappa, \dot{\kappa}) = \frac{\partial f_{\mathrm{vp}}}{\partial \boldsymbol{\sigma}} : \dot{\boldsymbol{\sigma}} + \frac{\partial f_{\mathrm{vp}}}{\partial \kappa}\dot{\kappa} + \frac{\partial f_{\mathrm{vp}}}{\partial \dot{\kappa}}\ddot{\kappa}. \tag{5}$$

This can be rewritten, using Equation (2), as

$$\frac{\partial f_{\text{vp}}}{\partial \boldsymbol{\sigma}} : \dot{\boldsymbol{\sigma}} - h\dot{\lambda} - s\ddot{\lambda} = 0, \tag{6}$$

where

$$h = -\frac{\partial f_{\text{vp}}}{\partial \kappa} k(\boldsymbol{\sigma}, \kappa) - \frac{\partial f_{\text{vp}}}{\partial \dot{\kappa}} \dot{k}(\boldsymbol{\sigma}, \kappa), \tag{7}$$

$$s = -\frac{\partial f_{\text{vp}}}{\partial \dot{\kappa}} k(\boldsymbol{\sigma}, \kappa) \tag{8}$$

are the generalized plastic and viscoplastic moduli, respectively. The consistency condition is now a first order differential equation for $\dot{\lambda}$. However, in the algorithmic treatment of the model, the rate of the internal variable is eliminated by approximation $\dot{\kappa} \approx k\Delta\lambda/\Delta t$. Thereby, the standard methods of computational rate-independent plasticity can be applied in the numerical implementation of the model. This issue will be treated in detail later in this paper.

As for the selection of the yield function (or criterion), the work by Colmenares and Zoback [7] is taken as a starting point. They evaluate statistically seven intact rock failure criteria against polyaxial data of five different rocks. The criteria they study are the Mohr-Coulomb, Hoek-Brown, Drucker-Prager, Modified Lade, Modified Wiebols and Cook, and empirical Mogi 1961 and 1971 criteria. According to their findings, the polyaxial Modified Wielbols and Cook and Modified Lade criteria fit well most of the test data, especially for the rocks with a high intermediate stress (σ_2) dependency (Dunham Dolomite and Solnhofen limestone). However, the Mohr-Coulomb and Hoek-Brown criteria, which neglect the influence of the intermediate stress, fit the data equally well (or even better) than the more complex criteria with rocks that do not show strong σ_2-dependency (Shirahama sandstone and Yuubari shale). Therefore, the polyaxial criteria may be dropped from the list of candidates due to their complexity and questionable benefit with respect to accuracy for some rocks. The final selection is to be done between the Mohr-Coulomb and te Hoek-Brown criteria.

The Hoek-Brown (HB) criterion, developed originally by Hoek and Brown [4], is a nonlinear, allegedly empirical strength criterion developed primarily from the test data for application to excavation design. This criterion better matches the experimental data of some rocks under quasi-static compression, especially in the highly confined region, than the widely used Mohr-Coulomb criterion (this follows from the fact that MC criterion is linear but the experimental strength envelopes of many rocks are nonlinear). The HB criterion is superior to MC criterion under dynamic loading conditions as well [6]. For these reasons, it is chosen as a yield function in this paper. In its generalized form for different rock types and masses the criterion reads [8]

$$\sigma_1 = \sigma_3 + \sigma_{\text{c}} \left(m\frac{\sigma_3}{\sigma_{\text{c}}} + s \right)^a, \tag{9}$$

where σ_1, σ_3 are the major and minor principal stresses, σ_{c} is the compressive strength while m, s and a are empirical parameters depending on the rock type, for details see [4] and [8]. For intact rock, which is considered here, $s = 1$, $a = 1/2$ and $m = -\sigma_{\text{c}}/\sigma_{\text{a}}$ with σ_{a} being the tri-axial (bi-axial in 2D) tensile strength. The HB criterion is illustrated in figure 1 in 2D case along with the MMC criterion (i.e. the MC with the Rankine criterion as a tension cut-off). As can observed in figure 1, the HB criterion predicts the bi-axial

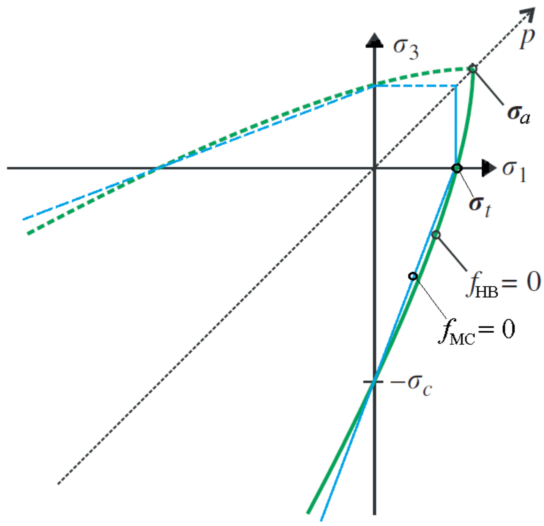

Figure 1. Hoek-Brown and modified Mohr-Coulomb criterions projected on the $\sigma_1 - \sigma_3$ plane.

tensile strength slightly higher than the uni-axial one. This feature may be questioned on physical grounds but such a discussion is beyond the scope of the present paper.

For present purposes, the viscoplastic yield function based on the HB criterion and the linear rate-dependent hardening softening rules for tensile and compressive strengths are written as

$$f_{\mathrm{HB}}(\boldsymbol{\sigma}, \lambda, \dot{\lambda}) = (\sigma_1 - \sigma_3)^2 + \sigma_{\mathrm{c}}(\lambda, \dot{\lambda})^2 \left(\frac{\sigma_1}{\sigma_{\mathrm{t}}(\lambda, \dot{\lambda})} - 1 \right), \tag{10}$$

$$\sigma_{\mathrm{t}} = \sigma_{\mathrm{t0}} + h_{\mathrm{t}}\lambda + s_{\mathrm{t}}\dot{\lambda}, \tag{11}$$

$$\sigma_{\mathrm{c}} = \sigma_{\mathrm{c0}} + h_{\mathrm{c}}\lambda + s_{\mathrm{c}}\dot{\lambda}. \tag{12}$$

In writing the yield function in (10), function k relating the internal variable and viscoplastic increment is taken unity for simplicity, i.e. $k(\boldsymbol{\sigma}, \kappa) \equiv 1$, giving $\kappa = \lambda$. Moreover, the model behavior is assumed to be perfectly viscoplastic, i.e. hence forward $h_{\mathrm{t}} = 0$ and $h_{\mathrm{c}} = 0$. This setting means that the strength (and stiffness) degradation or softening is governed by the damage part of model while the viscoplastic part incorporates the rate-dependency and indicates the stress states leading to damage. As for the viscosity moduli, s_{t}, s_{c}, they are assumed to be constants for simplicity and due to the lack of experimental data. Finally, associated plasticity is assumed here for simplicity, i.e. $g_{\mathrm{HB}} = f_{\mathrm{HB}}$.

A note on implementation economy related to the HB and MMC models is in order here. Namely, a model based on the HB criterion represents - more or less successfully - the asymmetric behavior of rock in tension and compression with a single surface whereas the MC criterion needs a tensile cut-off to mend its poor tensile strength prediction. This is a computational advantage as no corner plasticity situations appear in the numerical implementation of the model. The MMC criterion, in contrast to HB criterion, requires corner plasticity treatment at the non-smooth transition from the MC flow to the Rankine flow and *vice versa*, see figure 1. On the other hand, the MMC criterion is (piecewise) linear while the HB criterion is nonlinear needing thus an iterative return mapping method. Moreover, the computational efficiency of MMC criterion is considerably improved by Clausen et al. [9] (perfectly plastic case) and Saksala [10] (extension to linear softening/hardening). Still, from the simplicity's point of view (Occam's Razor could be invoked here), a criterion that matches the uniaxial tensile and compressive strengths of rock with a single mathematical expression is preferable to those requiring two expressions.

Before proceeding to the damage part of the model, is also reminded that the viscosity is incorporated in the present approach in order to regulate the ill-posed problem of classical strain softening continua (plasticity), i.e. viscosity provides a localization limiter. Moreover, the loading rate sensitivity can be nicely accommodated through viscosity. Hence, the viscosity moduli above do not represent any material property of rock - they are numerical parameters of the mathematical model.

Damage part of the model

The damage part of the model is formulated within the well established isotropic damage theory (see e.g. [3]) with separate scalar damage variables in tension and compression. In the present formulation, damage evolution is driven by the viscoplastic strain. Consequently, no damage loading function is needed. Thus, specification is needed only for the damage evolution laws and the equivalent viscoplastic strains that drive the damaging. Typical exponential damage evolution laws along with the equivalent viscoplastic strains in tension and compression, $\dot{\epsilon}^{\mathrm{vp}}_{\mathrm{eqvt}}$and $\dot{\epsilon}^{\mathrm{vp}}_{\mathrm{eqvc}}$, are employed here as

$$\omega_{\mathrm{t}} = A_{\mathrm{t}}(1 - \exp(\beta_{\mathrm{t}}\epsilon^{\mathrm{vp}}_{\mathrm{eqvt}})), \tag{13}$$

$$\omega_{\mathrm{c}} = A_{\mathrm{c}}(\sigma_{\mathrm{conf}})(1 - \exp(\beta_{\mathrm{c}}(\sigma_{\mathrm{conf}})\epsilon^{\mathrm{vp}}_{\mathrm{eqvc}})), \tag{14}$$

$$\dot{\epsilon}^{\mathrm{vp}}_{\mathrm{eqvt}} = \sqrt{\sum_{i=1}^{3}\langle\dot{\epsilon}^{\mathrm{vp}}_{i}\rangle^2_{+}}, \tag{15}$$

$$\dot{\epsilon}^{\mathrm{vp}}_{\mathrm{eqvc}} = \sqrt{\tfrac{2}{3}\dot{\boldsymbol{\epsilon}}^{\mathrm{vp}}_{\mathrm{dev}} : \dot{\boldsymbol{\epsilon}}^{\mathrm{vp}}_{\mathrm{dev}}}. \tag{16}$$

The positive part operator $\langle \mathbf{x}\rangle_{+} = \max(\mathbf{x}, 0)$ has been used on the rates of the viscoplastic principal strain components $\dot{\epsilon}^{\mathrm{vp}}_{i}$ in (15). Moreover, $\boldsymbol{\epsilon}^{\mathrm{vp}}_{\mathrm{dev}}$ is the deviatoric viscoplastic strain and parameters A_{t}, β_{t} in (13) and (14) control the maximum value of damage and the initial slope of damage evolution, respectively. In compression, parameters $A_{\mathrm{c}}, \beta_{\mathrm{c}}$ are functions of confining pressure σ_{conf} which is the lateral pressure in the triaxial compression test. In numerical simulations, it can be calculated as $\sigma_{\mathrm{conf}} = \frac{1}{2}(\sigma_1 + \sigma_2)$ if $\sigma_1 < 0$ (otherwise it is zero). The effect of confining pressure in the triaxial compression test depends on the rock type. This dependence is specified here for the Carrara marble following Fang and Harrison [11] and Saksala and Ibrahimbegovic [12]. Accordingly, these parameters depend on the confining pressure and the fracture energies as follows

$$A_{\mathrm{c}}(\sigma_{\mathrm{conf}}) = A_{\mathrm{c0}}\exp(-n_{\mathrm{d}}\sigma_{\mathrm{conf}}), \tag{17}$$

$$\beta_{\mathrm{c}}(\sigma_{\mathrm{conf}}) = \beta_{\mathrm{c0}}\exp(-n_{\mathrm{d}}\sigma_{\mathrm{conf}}), \tag{18}$$

$$\beta_{\mathrm{c0}} = \frac{\sigma_{\mathrm{c0}}h_{\mathrm{e}}}{G_{\mathrm{IIc}}}, \quad \beta_{\mathrm{t}} = \frac{\sigma_{\mathrm{t0}}h_{\mathrm{e}}}{G_{\mathrm{Ic}}}, \tag{19}$$

where n_{d} is an experimental parameter depending on the rock type and h_{e} is a characteristic length. In the FE context it is the element side length. This choice of making the amount of dissipation dependent on the mesh is justified by the fact that even though viscoplasticity provides a localization limiter for the ill-posed problem of classical softening continuum, the amount of dissipation needs to be tied to a material parameter which in the present case are the fracture energies G_{Ic} and G_{IIc}. The model thus defined predict the correct amount of dissipation in uniaxial tension and compression irrespective of the mesh refinement. Moreover, as a result of equation (18), the maximum value of the compressive damage of the rock sample in confined compression decreases (exponentially) as confinement increases. This in turn means that the residual strength of of the sample increases as a function of confining pressure. Therefore, the model is able to predict the confining pressure dependent brittle-to-ductile transition exhibited by compact carbonate rocks such as marble and limestone.

Finally, the nominal-effective stress relation addressing the unilateral conditions related to microcrack closure and opening as

$$\boldsymbol{\sigma} = (1 - \omega_{\mathrm{t}})\bar{\boldsymbol{\sigma}}_{+} + (1 - \omega_{\mathrm{c}})\bar{\boldsymbol{\sigma}}_{-}, \tag{20}$$

where the positive-negative part split of the principal effective stress $\bar{\boldsymbol{\sigma}}$ has been used with $\bar{\boldsymbol{\sigma}}_{+} = \max(\bar{\boldsymbol{\sigma}}, 0)$ and $\bar{\boldsymbol{\sigma}}_{-} = \min(\bar{\boldsymbol{\sigma}}, 0)$.

Solving the stress for a finite element

The solution method for the stress at an integration point of a finite element is presented in this subsection for the convenience of the reader. The combination of the viscoplastic and damage parts of the model is based on the effective stress space formulation since it allows for a separation of the (visco)plasticity and damage computations and facilitates thus the implementation.

The stress return mapping is based on the cutting plane algorithm described e.g. in Simo and Hughes [13]. At the end of a time step, condition $f_{\mathrm{HB}}(\boldsymbol{\sigma}_{t+\Delta t}, \lambda_{t+\Delta t}, \dot{\lambda}_{t+\Delta t}) = 0$ must be satisfied. Now, following assumptions are used to eliminate the internal variable and its rate at the end of the time step

$$\lambda_{t+\Delta t} = \lambda_t + \Delta\lambda_{t+\Delta t}, \quad \dot{\lambda}_{t+\Delta t} = \Delta\lambda_{t+\Delta t}/\Delta t. \tag{21}$$

With these relations, the condition to be fulfilled becomes $f_{\mathrm{HB}}(\boldsymbol{\sigma}_{t+\Delta t}, \Delta\lambda_{t+\Delta t}) = 0$. This can be expanded with the first term of Taylor series to obtain the algorithmic increment $\delta\lambda$ (dropping the subscript $t + \Delta t$ and the dependency on the stress for brevity) as

$$f_{\mathrm{HB}}(\Delta\lambda) + \partial_{\Delta\lambda} f_{\mathrm{HB}}(\Delta\lambda)\delta\lambda = 0 \Leftrightarrow \delta\lambda = G^{-1} f_{\mathrm{HB}}(\Delta\lambda) \tag{22}$$

$$\text{with} \quad G = -\partial_{\Delta\lambda} f_{\mathrm{HB}}(\Delta\lambda) = \frac{\partial f_{\mathrm{HB}}}{\partial \boldsymbol{\sigma}} : \mathbf{E} : \frac{\partial f_{\mathrm{HB}}}{\partial \boldsymbol{\sigma}} - \mathbf{q} \cdot \mathbf{s}, \tag{23}$$

$$\mathbf{q} = [-\frac{\sigma_{\mathrm{c}}^2}{\sigma_{\mathrm{t}}}\sigma_1,\ 2\sigma_{\mathrm{c}}\left(\frac{\sigma_1}{\sigma_{\mathrm{t}}} - 1\right)]^{\mathrm{T}}, \tag{24}$$

$$\mathbf{s} = \frac{1}{\Delta t}[s_t,\ s_c]^{\mathrm{T}}. \tag{25}$$

As the HB criterion is expressed in terms of principal stresses, the stress return mapping is performed in the principal stress space. Next, the main steps of the return mapping utilizing the standard elastic predictor-(visco)plastic corrector split are presented assuming the plastic case is realized, i.e. $f_{\mathrm{HB}}^{\mathrm{trial}} = f_{\mathrm{HB}}(\boldsymbol{\sigma}_{\mathrm{trial}}, \lambda_t, \dot{\lambda}_t) > 0$ with $\boldsymbol{\sigma}_{\mathrm{trial}} = \mathbf{E} : (\boldsymbol{\epsilon}_{t+\Delta t} - \boldsymbol{\epsilon}_t^{\mathrm{vp}})$:

$$\delta\lambda_n = \frac{f_{\mathrm{HB}}^n}{\frac{\partial f_{\mathrm{HB}}^n}{\partial \boldsymbol{\sigma}_n} : \mathbf{E} : \frac{\partial f_{\mathrm{HB}}^n}{\partial \boldsymbol{\sigma}_n} - \mathbf{q}_n \cdot \mathbf{s}}, \tag{26}$$

$$\Delta\lambda_{n+1} = \Delta\lambda_n + \delta\lambda_n, \tag{27}$$

$$\boldsymbol{\epsilon}_{n+1}^{\mathrm{vp}} = \boldsymbol{\epsilon}_n^{\mathrm{vp}} + \delta\lambda_n \frac{\partial f_{\mathrm{HB}}^n}{\partial \boldsymbol{\sigma}_n}, \tag{28}$$

$$\boldsymbol{\sigma}_{n+1} = \boldsymbol{\sigma}_n + \delta\lambda_n \mathbf{E} : \frac{\partial f_{\mathrm{HB}}^n}{\partial \boldsymbol{\sigma}_n}, \tag{29}$$

$$\sigma_{\mathrm{t},n+1} = \sigma_{\mathrm{t0},n} + s_{\mathrm{t}} \frac{\Delta\lambda_{n+1}}{\Delta t}, \tag{30}$$

$$\sigma_{\mathrm{c},n+1} = \sigma_{\mathrm{c0},n} + s_{\mathrm{c}} \frac{\Delta\lambda_{n+1}}{\Delta t}. \tag{31}$$

These steps are repeated until $f_{\mathrm{HB}}^n < TOL$ where TOL is the convergence tolerance. After the stress update is performed, the equivalent viscoplastic strains and the damage variables are updated based on Equations (13) - (16). Finally, the nominal stress is calculated by Equation (20). The nominal stress is then used for calculation of the internal force vector at the integration point of a finite element as $\mathbf{f}_{\mathrm{int}}^e = \int_{dV} \mathbf{B}^{\mathrm{T}} \boldsymbol{\sigma}_e dV$ with $\mathbf{B}$ being the kinematic matrix.

Solving the equations of motion

The material model for rock presented above is implemented with the FE method (spatial discretization). As the aim is to simulate transient dynamic problems involving impact and stress wave propagation, in addition to quasi-static tests, the equations of motion are discretized explicitly in time. The mofidied Euler method is chosen for this end. Accordingly, the response (velocity and displacement) of the system is predicted as follows

$$\ddot{\mathbf{u}}^t = \mathbf{M}^{-1}(\mathbf{f}_{\mathrm{ext}}^t - \mathbf{f}_{\mathrm{int}}^t), \tag{32}$$

$$\dot{\mathbf{u}}^{t+\Delta t} = \dot{\mathbf{u}}^t + \Delta t \ddot{\mathbf{u}}^t, \tag{33}$$

$$\mathbf{u}^{t+\Delta t} = \mathbf{u}^t + \Delta t \dot{\mathbf{u}}^{t+\Delta t}, \tag{34}$$

where $\mathbf{M}$ is the lumped mass matrix, and $\mathbf{u}, \dot{\mathbf{u}}, \ddot{\mathbf{u}}$ are the displacement, velocity and acceleration vector respectively.

Statistical description of rock strength

Rock is a heterogeneous material consisting of different minerals with different material properties, orientation and size. This heterogeneity leads to the statistical nature of rock and is the major feature influencing rock fracture processes through the formation, extension and coalescence of microcracks. Therefore, heterogeneity should be taken into account in numerical modeling aiming at realistic prediction, see e.g. [14]. Generally, the numerical description of rock microstructure depends, at least to some extent, on the chosen modeling approach.

In the present continuum approach based on finite elements, the simplest method to account for rock strength heterogeneity is to assume the strength properties to be statistically distributed element-wise. Here the method originally presented by Tang [15] is followed. Accordingly, the uniaxial compressive strengh of rock is assumed to be Weibull distributed. The three-parameter Weibull propability distribution function reads

$$\mathrm{Pr}(x) = 1 - \exp\left(-\frac{x - x_{\mathrm{u}}}{x_0}\right)^{m_{\mathrm{w}}}, \tag{35}$$

where, in the mechanics context, the shape parameter m_{w} is interpreted as the homogeneity index, the scale parameter x_0 is taken as the average (measured) value of the material property, and the location parameter x_{u} specifies the lower value of the material property.

Spatial distribution of the strength of rock represented by a finite element mesh is obtained after assigning a single number ($\mathrm{Pr}(x)$) from uniformly distributed random data between 0 and 1 to each element in the mesh and then solving x from equation (35).

Numerical examples

The performance of the model developed above is demonstrated with various numerical simulation in both finite element and laboratory sample level. The material and model parameters used in all simulations are given in table 1. They are valid for Carrara marble with the exception that the mode I and II fracture energies are for Ekeberg marble.

Table 1. Material properties and model parameters for material point level simulations.

Quantity Unit	E GPa	σ_{t0} MPa	σ_{c0} MPa	ν	ρ kg/m^3	n_{d}	G_{Ic} N/m	G_{IIc} N/m	A_{t}	A_{c0}
Value	60	14	140	0.274	2600	0.03	0.04	1.5	0.98	0.9

Material point level simulations

The material point level simulations are carried out here in order to demonstrate the model behavior. The mesh consisting of two constant strain triangle (CST) elements and boundary conditions illustrated in figure 2 are used. In the first simulation, the model response in cyclic loading is tested. In the second simulation, the confined compression test is simulated while the third and fourth simulation demonstrate the rate effect in uniaxial tension and compression. The viscosity parameters are set as $s_{\mathrm{c}} = s_{\mathrm{t}} = 10\,\mathrm{MPas}$ and the element characteristic length is calculated as $h_{\mathrm{e}} = \sqrt{2A_{\mathrm{e}}}$, A_{e} being the area of an element. The results are shown in figure 3.

From the results in figure 3a, it is observed that the peak stress increases nonlinearly as a function of confining pressure. Predictions with the MC criterion exhibiting a linear increase of the peak stress are indicated by arrows. Figure 3b shows the model response in cyclic loading starting with tension cycle after which compression takes place and, finally, the load returns to tension. It should be noticed that both damage variables grow (see figure 3c) during tension and compression phases of the loading due to the chosen equivalent viscoplastic strains (Equations (15), (16)). In tension the damage growth is faster and reaches the maximum value 0.98 already during the compression cycle. This is justified by the fact that a fully developed shear band in geomaterials cannot sustain any tensile loading in its normal direction. Therefore, tensile damage should always grow

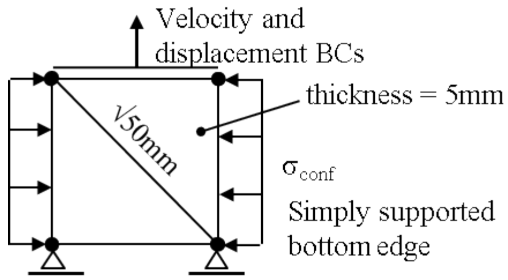

Figure 2. Computational model for material point level simulations.

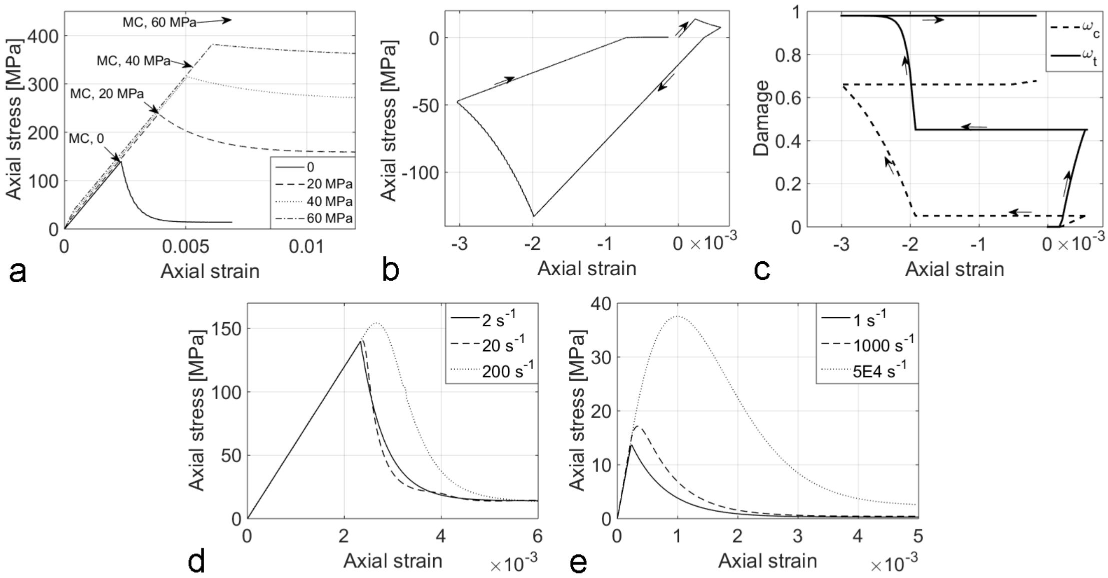

Figure 3. Simulation results for material point level simulations: confined compression test (a), cyclic loading response (b), damage evolution in cyclic loading (c), influence of loading rate in compression (d), and in tension (e).

in conjunction with the compressive (shear) damage. The reciprocal process, i.e. the compressive damage development in tensile loading, seems unphysical. However, this process is much slower as can be observed in figure 3c.

As for the strain rate effects, the model does not perform very well neither in compression nor in tension. In compression, higher loading rates than those in figure 3d resulted in a non-stable response. This is, at least partly, due to the inconvenient feature of the HB criterion that the compressive strength appears squared in it. In tension, the model response is typical for viscoplastic models, see figure 3e, but extremely high strain rates were required to produce the strain rate hardening effects. While this is partly due to relatively low values of viscosity moduli used here, the more important reason seems to be the unfavorable appearance (in denominator) of the rate-dependent tensile strength in the Hoek-Brown criterion (10). The classical criteria such as Rankine, Drucker-Prager and Mohr-Coulomb, have form $f(\boldsymbol{\sigma}, \kappa, \dot{\kappa}) = \hat{f}(\boldsymbol{\sigma}) + \sigma_Y(\kappa, \dot{\kappa})$ where $\hat{f}(\boldsymbol{\sigma})$ is some expression of stress. As the yield stress, σ_Y, usually depends linearly on $\kappa, \dot{\kappa}$, these models perform much better, see e.g. [14].

Laboratory sample level: confined compression and uniaxial tension tests on rock

The confined compression and uniaxial tension tests on rock are simulated in order to test the model predictions at the structural level. The mesh made of CST elements along with the boundary conditions are shown in figure 4a. An example of UCS distribution produced with the Weibull approach described above when $m_\mathrm{w} = 3$, $x_0 = 140$ MPa, and $x_\mathrm{u} = 50$ MPa is shown in figure 4b. This value 3 for Weibull shape modulus m_w, called homogeneity index by Zhu and Tang [16], is the middle one tested by them. The other values they tested were 1.5 and 6 where the first makes the rock too soft as the strength (or any other material property) is too widely distributed while the second one makes the rock more homogeneous and overly brittle- actually too brittle in the case of marble modeled here.

As seen in figure 4b, the UCS of the numerical sample varies dramatically from element to element the lower limit being 50 MPa and the upper about 300 MPa. However, this is the case in reality as well since the rock microstructure is a complex network of microdefects and grains of different minerals with highly varying material properties. Thus, the pointwise variation of UCS from a hard mineral grain, such as quartzite, in a rock to a neighboring softer mineral grain or microflaw may easily reach the magnitude of 250 MPa. The UCS of a rock then, which for the present case is 140 MPa, is a macroscopic laboratory level property emerging from the microstructural properties. More detailed elaboration on this topic is, however, beyond the scope of the present paper and is left to be investigated in future studies. In the numerical simulations, the effect of m_w is that lower values (than 3 here) make the rock response more nonlinear and ductile and lead to considerably lower strengths while higher values (than 3 here) make the rock more brittle and linear with increased strengths [16].

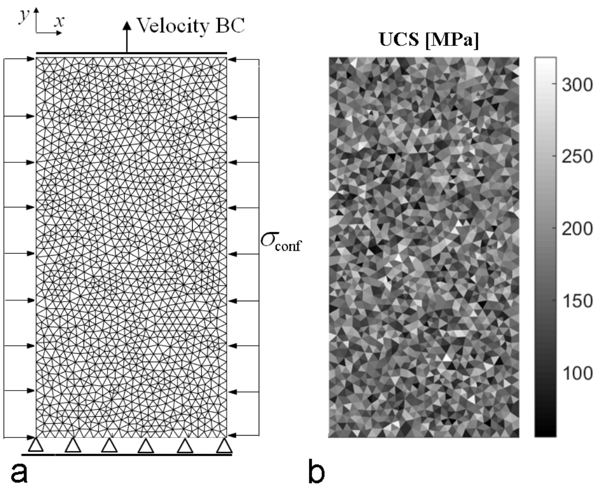

Figure 4. Computational model (dimensions 25 × 50 mm for confined compression test simulation (2702 CST elements in the mesh) (a), and an example of UCS distribution in the mesh (b).

The simulations are carried out in the unconfined case and at pressure levels 20 and 40 MPa. A new distribution of UCS is generated for each simulation. Moreover, the uniaxial tensile strength distribution is obtained from the UCS distribution after multiplying it by $m^{-1} = 0.1$ (inverse of the HB parameter). The constant boundary velocity applied is $v = -0.1\mathrm{m/s}$. The results along with some experimental failure modes are shown in figure 5. The predicted failure modes at different levels of confinement exhibit typical features

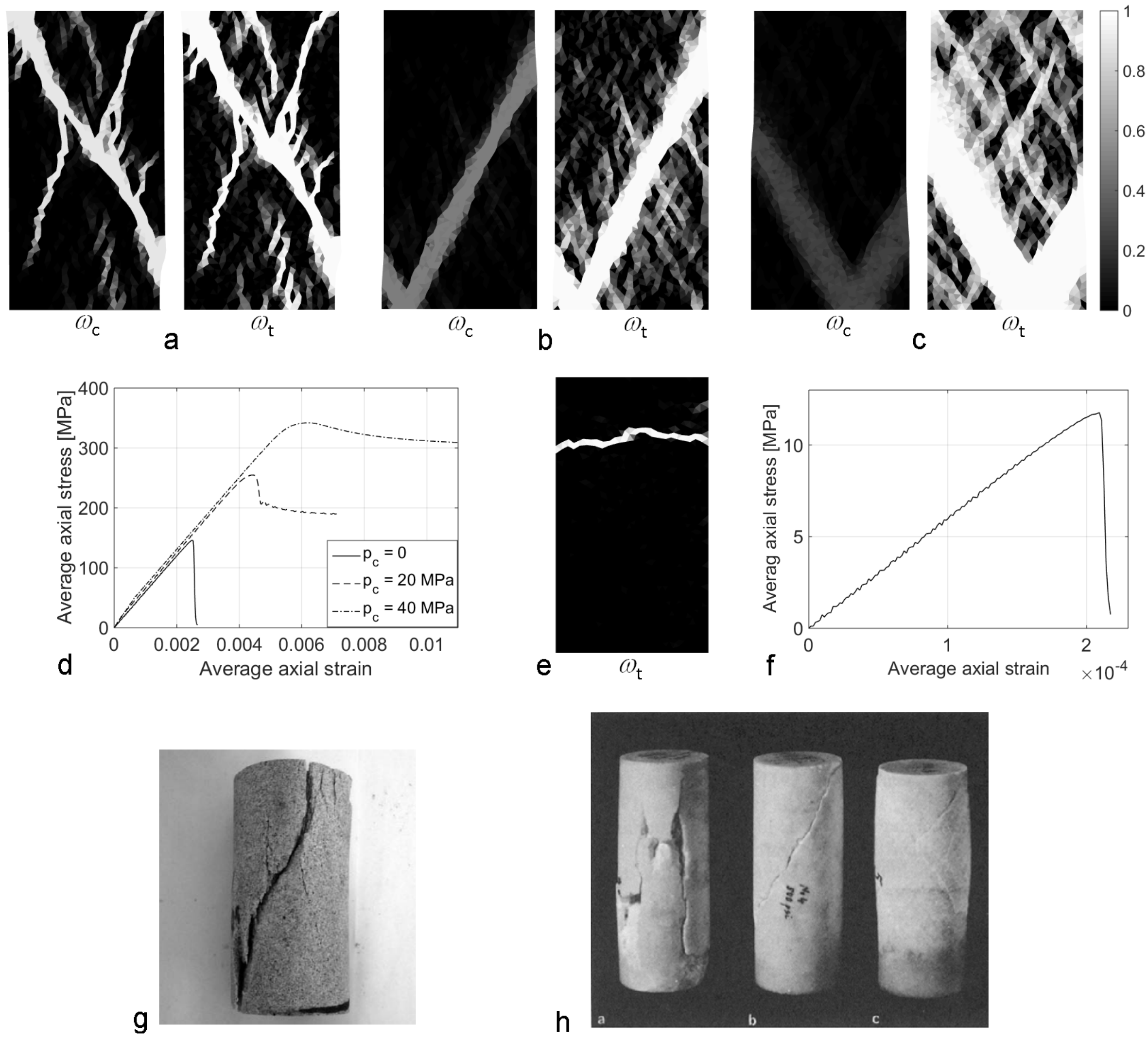

Figure 5. Simulation results for confined compression and uniaxial tension tests: Damage patterns when $p_{\text{conf}} = 0\,\text{MPa}$ (a), $p_{\text{conf}} = 20\,\text{MPa}$ (b), $p_{\text{conf}} = 40\,\text{MPa}$ (c), corresponding stress-stress curves (d), tensile damage pattern in uniaxial tension (e), and the stress-stress curve (f), experimental failure mode in uniaxial test (Adapted from [18]) (g), and experimental failure modes of Wombeyan marble in confined compression with 0, 3.5, and 35 MPa of confining pressure (Adapted from [17]) (h).

observed in the experiments, as can be seen in figure 5h. More specifically, the unconfined failure mode has a major slanted macrocrack spanning the specimen but there are other minor vertical cracks deviating from the major crack. This simulated failure mode is, by chance of course, very close to the experimental one shown in figure 5g. Under confinement of 20 MPa this secondary tensile crack formation is mostly suppressed resulting in a single shear band (see figure 5b) which is thicker than the major crack in the unconfined case. Upon still increasing confinement to 40 MPa, the manifested failure mode is the typical conjugate crack system (compare figure 5c to 5h) attested many times in the experiments with marble rocks. As for the corresponding stress-strain responses, the new features appeared at the structural level are pre-peak nonlinearity and rounded peak part of the response. These are due to the statistical UCS distributions as the weak rock elements start to fail beyond stress level 50 MPa (the value of Weibull location parameter). This is a numerical representation of microcracking in the experiments. Therefore, using the statistical distribution of UCS, or some other method, is necessary for realistic modeling of rock failure phenomena in confined compression. The transverse splitting failure mode in uniaxial tension (simulation carried out with $v = 0.01$ m/s) is also correctly predicted (see figure 5e). Finally, the predicted statistical tensile strength is 11.8 MPa.

Laboratory sample level: dynamic three-point bending of a notched semi-circular disc

Dynamic bending test of a Notched Semi-Circular disc (NSC) using the Split Hopkinson Pressure Bar (SHPB) device is used for measuring rock dynamic fracture toughness. The principle of the computational model illustrated in figure 6 is as follows. The compressive stress wave induced by impacting striker bar is simulated as an external stress pulse, $\sigma_{\rm i}(t)$. The incident and transmitted bars are modeled with two-node standard bar elements, and the NSC disc is meshed with the CST elements. Finally, the contacts between the bars and the half disc are modeled by imposing kinematic contact constraints between the bar end nodes and the half disc nodes at the support support pins ($P_2/2$). These constraints are of form $u_{{\rm bar},z} - u_{n,z} = b_n$ where $u_{{\rm bar},z}$ and $u_{n,z}$ are the axial degrees of freedom of the bar node and a rock contact node n, respectively, and b_n is the distance between the bar end and rock boundary node. The contact constraints are imposed with the forward increment Lagrange multiplier method (for details see [14]). The dimensions of the half disc are 16

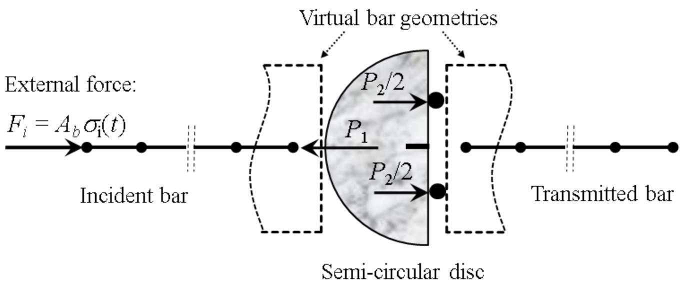

Figure 6. Computational model for dynamic three-point bending of notched semi-circular disc test simulation.

mm (thickness) and 40 mm (diameter) while the depth and the width of the notch are 4 mm and 1 mm, respectively. The distance between the supporting pins is 21 mm in present simulations. The incident and transmitted bar lengths and diameters are 1200 mm and 25 mm, respectively. In each simulation, a sine-pulse is applied as $\sigma_{\rm i}(t) = A_{\rm p}\sin(\omega t)$ where $A_{\rm p} = 100$ MPa, t is time, $\omega = 2\pi/T$ with $T = 160\,\mu s$. The Weibull parameters are as above. Finally, the viscosity moduli are set to $s_{\rm c} = s_{\rm t} = 0.01$ MPas. The simulation results are shown in figure 7.

According to the results in figure 7, the predicted failure mode is the axial splitting of the disc into two halves which rotate about the contact point between the specimen and the incident bar reported, e.g. in [19], and shown also in figure 7e on Flamboro limestone. The damage patterns attest a single macrocrack propagating from the notch and reaching the contact area where some secondary crack formation occurs due to high contact pressure. Moreover, some tensile damaging at the contact pin areas can be observed. The corresponding contact force curves are roughly similar but the curve for P_1 clearly display failure events at the contact area realized as a sudden drop in the curve. Finally, the previous simulation is repeated with higher amplitude $A_{\rm p} = 150$ MPa. The results are shown

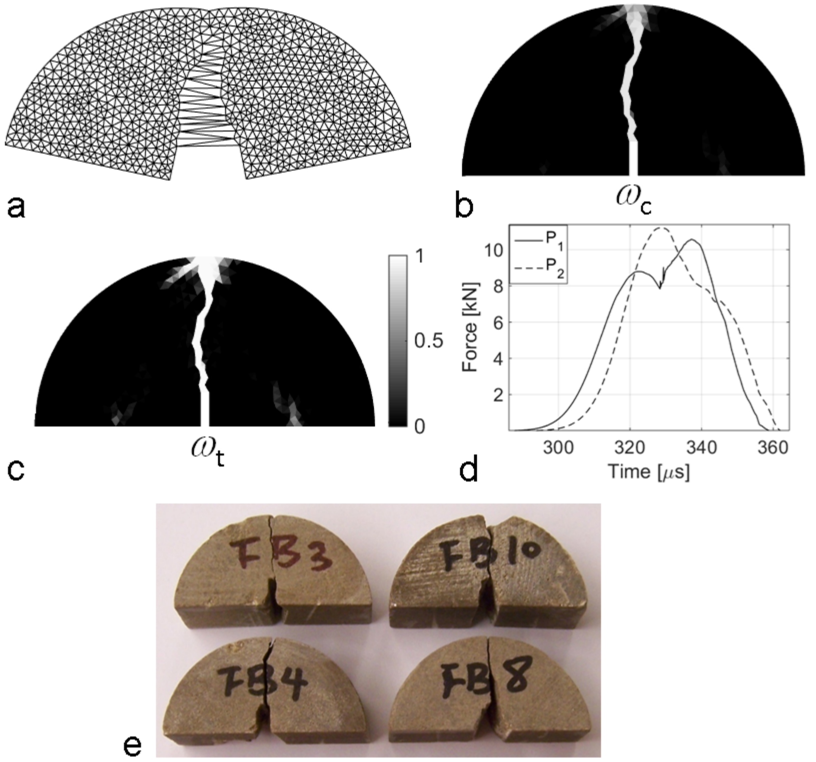

Figure 7. Simulation results for dynamic 3-point bending of NSC (pulse amplitude 100 MPa): Deformed mesh (1773 elements, magnification = 10) (a), compressive damage pattern (b), tensile damage pattern (c), the contact forces as function of real time (d), and the experimental failure modes of Flamboro limestone (Courtesy of Prof. K. Xia) (e).

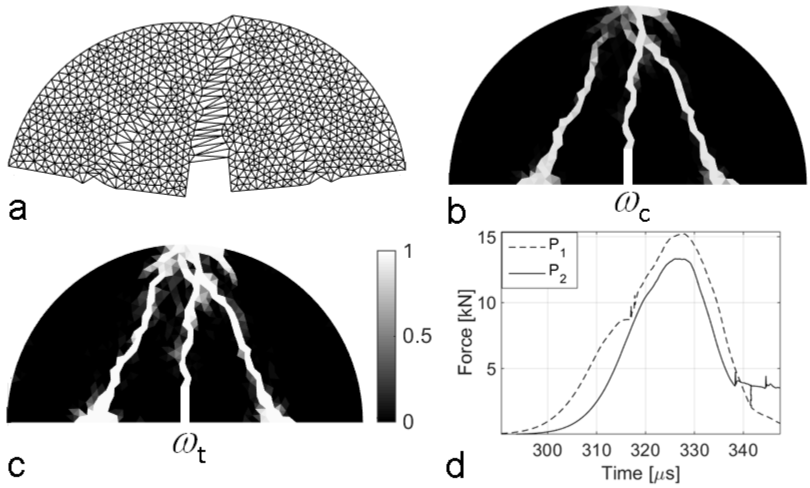

Figure 8. Simulation results for dynamic 3-point bending of NSC (pulse amplitude 150 MPa): Deformed mesh (a), compressive damage pattern (b), tensile damage pattern (c), and the contact forces as function of real time (d).

in figure 8. With the higher amplitude stress pulse, the predicted failure mode exhibits secondary cracks initiating at the contact areas of the support pins of transmitted bar and propagating to the contact area of the incident bar, see figure 8. These cracks may be observed in the experiments but the measurements are not valid anymore since they are based on the assumption that a macrocrack leading to the failure of the sample initiate at the tip of the notch. In the present simulation this is not the case as the contact forces are not equal, i.e. there is no "dynamic equilibrium" as can be observed in figure 8d.

Conclusions

A damage-viscoplastic model for numerical modeling of rock fracture was presented in this paper. As the viscoplastic part was formulated with the empirical Hoek-Brown criterion, the model predicts the failure strengths of some rocks under confined compression test more accurately than the classical linear (in confinement) criteria, such as Drucker-Prager or Mohr-Coulomb criteria. Moreover, these classical criteria usually need a tension cut-off whereas the Hoek-Brown criterion matches both the uniaxial tensile and compressive strengths with a single surface - a computational advantage - due to its nonlinearity. However, the same nonlinearity requires iterative stress integration which is a computational loss in comparison to the linear criteria. Moreover, the present formulation of the Hoek-Brown criterion where both the compressive and tensile strengths appear explicitly as functions of hardening/softening variables and their rates, resulted in a model which does not predict strain rate effects as well as the mentioned linear models. This was observed in numerical simulations at different loading rates.

The model, nevertheless, predicts the experimental failure modes of rock under quasi-static confined compression and uniaxial tension with a reasonable accuracy. The crucial feature in this respect is the statistical description, using the Weibull distribution, of rock strength heterogeneity. In the simulation of dynamic three-point bending of a notched semi-circular disc, the model predicted the correct failure mode initiated at the notch tip. However, due to the problems in predicting strain-rate effects, some other technique to accommodate the strain rate-effects (where they cannot be neglected) should be searched. Alternatively, the damage-plasticity model based on the Hoek-Brown criterion can be applied to rate-independent problems.

Finally, it is noted that the strategy to extend the underlying plasticity model to account for damaging and rate-effects does not depend specifically on the chosen Hoek-Brown criterion but can be applied to any yield criterion. Development of the formal framework of this extension applied to general yield criterion could be a subject of further research.

Acknowledgments

Prof. Kaiwen Xia from the Impact and Fracture Laboratory of University of Toronto (Canada) is gratefully acknowledged for providing the experimental failure modes in dynamic bending of semicircular discs made of Flamboro limestone.

References

[1] L. Jing and J.L. Hudson. Numerical methods in rock mechanics. *International Journal of Rock Mechanics & Mining Sciences*, 39(4):409–427,2002. doi:10.1016/S1365-1609(02)00065-5

[2] W.M. Wang, L.J. Sluys, R. De Borst. Viscoplasticity for instabilities due to strain softening and strain-rate softening. *International Journal for Nu-*

merical Methods in Engineering, 40:3839–3864,1997. doi:10.1002/(SICI)1097-0207(19971030)40:20<3839::AID-NME245>3.0.CO;2-6

[3] J. Lemaitre. *A Course on Damage Mechanics*, Springer-Verlag, 1990.

[4] E. Hoek, E.T. Brown. Empirical strength criterion for rock masses. *Journal of the Geotechnical Engineering Division ASCE*. 106(9):1013–1035,1980.

[5] P. Grassl, M. Jirasek. Damage-plastic model for concrete failure. *International Journal of Solids and Structures*. 43:7166–7196,2006. doi:10.1016/j.ijsolstr.2006.06.032

[6] J. Zhao. Applicability of Mohr-Coulomb and Hoek-Brown strength criteria to the dynamic strength of brittle rock. *International Journal of Rock Mechanics and Mining Sciences*. 37:1115–1121, 2000. doi:10.1016/S1365-1609(00)00049-6

[7] L.B. Colmenares, M.D. Zoback A statistical evaluation of intact rock failure criteria constrained by polyaxial test data for five different rocks. *International Journal of Rock Mechanics and Mining Sciences*. 39:695–729, 2002. doi:10.1016/S1365-1609(02)00048-5

[8] E. Hoek, C. Carranza-Torres, B. Corkum. *Hoek-Brown failure criterion – 2002 Edition*, Proc. NARMS-TAC Conference, Toronto, 2002, 1, 267-273.

[9] J. Clausen, L. Damkilde, L. Andersen. An efficient return algorithm for nonassociated plasticity with linear yield criteria in principal stress space. *Computers and Structures* 85:1795–1807, 2007. doi:10.1016/j.compstruc.2007.04.002

[10] T. Saksala. Geometric return algorithm for non-associated plasticity with multiple yield planes extended to linear softening/hardening models *Rakenteiden Mekaniikka (Journal of Structural Mechanics)* 42:83-98, 2009.

[11] Z. Fang, J.P. Harrison. A mechanical degradation index for rock. *International Journal of Rock Mechanics and Mining Sciences*. 38:1193–1199, 2001. doi:10.1016/S1365-1609(01)00070-3

[12] T. Saksala, A. Ibrahimbegovic. Anisotropic viscodamage-viscoplastic consistency constitutive model with a parabolic cap for rocks with brittle and ductile behaviour. *International Journal of Rock Mechanics and Mining Sciences*. 70:460–473, 2014. doi:10.1016/j.ijrmms.2014.05.019

[13] J.C. Simo, T.J.R. Hughes. *Computational Inelasticity*. Springer Verlag, New York, 1998.

[14] T. Saksala. Damage-viscoplastic consistency model with a parabolic cap for rocks with brittle and ductile behavior under low-velocity impact loading. *International Journal for Numerical and Analytical Method in Geomechanics*. 34:1041–1062, 2010. doi:10.1002/nag.847

[15] C.A. Tang. Numerical simulation of progressive rock failure and associated seismicity. *International Journal of Rock Mechanics and Mining Sciences*. 34:249–261, 1997. doi:10.1016/S0148-9062(96)00039-3

[16] W.C. Zhu, C.A. Tang. Micromechanical Model for Simulating the Fracture Process of Rock. *Rock Mechanics and Rock Engineering*. 37:25–56, 2004. doi:10.1007/s00603-003-0014-z

[17] M.S. Paterson. Experimental deformation and faulting in Wombeyan marble. *Geological Society of America Bulletin*. 69:465–76.

[18] Y. Zhou, J. Zhao In: J. Zhao (Ed.), Advances in Rock Dynamics and Applications *Chapter 1. Introduction*. CRC Press, 2011.

[19] R. Chen, K. Xia, F. Dai, F. Lub, S.N. Luo. Determination of dynamic fracture parameters using a semi-circular bend technique in split Hopkinson pressure bar testing. *Engineering Fracture Mechanics*. 76:1268–1276. doi:10.1016/j.engfracmech.2009.02.001

Timo Saksala
Department of Mechanical Engineering and Industrial Systems
Tampere University of Technology
P.O.Box 589, FIN-33101, Tampere, Finland
`timo.saksala@tut.fi`